IEEE Access
Multidisciplinary ⋮ Rapid Review ⋮ Open Access Journal

Received 3 December 2023, accepted 14 December 2023, date of publication 22 December 2023, date of current version 3 January 2024.

Digital Object Identifier 10.1109/ACCESS.2023.3346317

RESEARCH ARTICLE

Alternate Rotor Design for Line-Start Synchronous Reluctance Motor With Minimum Use of Copper

MOEIN FARHADIAN[1], MEHDI MOALLEM[1], (Senior Member, IEEE), BABAK FAHIMI[2], (Fellow, IEEE), BEHZAD MIRZAEIAN DEHKORDI[3], AND MEHDI SAHEBZAMANI[4]

[1]Department of Electrical and Computer Engineering, Isfahan University of Technology, Isfahan 8415683111, Iran
[2]Department of Electrical and Computer Engineering, The University of Texas at Dallas, Richardson, TX 75080, USA
[3]Department of Electrical Engineering, University of Isfahan, Isfahan 81746-73441, Iran
[4]Kia Electromotor Part (KEP), Tehran, Iran

Corresponding author: Babak Fahimi (fahimi@utdallas.edu)

ABSTRACT Line-start synchronous reluctance motors (LSSynRM) combine the high efficiency of synchronous reluctance Motors (SynRM) with the self-starting capability of induction motors. They operate at synchronous speed in steady state and produce minor rotor losses, thereby providing higher efficiency than induction motors and a higher power density. Despite the simple structure of LSSynRM, its analysis, modeling, and optimal design pose several challenges. In particular, design trends aiming at higher starting capabilities and improved steady-state operation pose significant hurdles. In this study, three synchronous reluctance motors with line-start capability are designed to achieve maximum efficiency at steady-state operation with the optimum amount of copper for starting. The induction cage is constructed using rectangular bars installed in flux barriers to minimize the changes in performance under the steady-state condition. Although different rotor shapes offer similar steady-state performance, they achieve synchronism using different cage bar widths. The rotor with the lowest copper weight is selected for manufacturing. The prototype is constructed based on the optimal design. The experimental results are in good agreement with the simulation results.

INDEX TERMS Induction cage, line-start synchronous reluctance motor, rectangular bar, synchronization.

NOMENCLATURE

L_{sd}	d-axis inductance.
L_{sq}	q-axis inductance.
p	Pole pairs.
δ_i	Current angle relative to q-axis.
I	Stator current.
X_d	d-axis reactance.
X_q	q-axis reactance.
R_s	Stator phase resistance.
δ_v	Voltage angle relative to q-axis.
V	Voltage.
s	Slip.
ω	Synchronous angular speed.
γ	Phase of the pulsating torque components.
V_s	Stator Voltage.
R_{rd}	Rotor d-axis resistance.
R_{rq}	Rotor q-axis resistance.
L_{md}	d-axis magnetization inductance.
L_{mq}	q-axis magnetization inductance.
ω_r	Rotor angular speed.
W_{qi}	i_{th} flux barrier width along q-axis.
W_{di}	i_{th} flux barrier width along d-axis.
$\Delta\alpha_i$	i_{th} flux barrier angle along q-axis.
n_r	Number of rotor virtual slots per pole pairs.
n_s	Number of stator slots per pole pairs.
K_{insq}	Insulation ratio along q-axis.

The associate editor coordinating the review of this manuscript and approving it for publication was Pinjia Zhang.

I. INTRODUCTION

Line-start synchronous reluctance motor (LSSynRM) is a hybrid fusion of a synchronous reluctance motor (SynRM) and an induction motor (IM). The direct-on-line SynRM (DOLSynRM) [1] and Synduction motor [2] are alternate names used in the literature for this machine. Achieving a satisfactory performance during startup and steady state is the main objective in the design of LSSynRM. Notably, there are commercially available LSSynRMs in the market, such as Motovario self-starting synchronous reluctance motors. Understandably, their applications are limited due to their low moment of inertia of the load.

It is also important to note that although the power factor of the LSSynRM is lower than that of induction motor, its higher efficiency more than compensates for the additional losses in the cabling and in line transformers. Interested readers are referred to [2] and [5] where a detailed comparison of the two motors is presented.

Although LSSynRMs have a lower power factor compared to IMs, their efficiency is higher. The parameter $(1/(PF^*\eta))$ which is relative to the input current is less for the LSSynRM, so the supply cable loss is lower in the case of LSSynRM. In the case of large motors, the low power factor can be compensated by installing capacitor banks to reduce power loss in the supply cable.

The design methods of LSSynRM are divided into two main categories where emphasis is placed on induction rotor [3], [4] or on the reluctance rotor [5], [6].

The initial LSSynRM designs include an induction-type rotor with embedded flux barriers (FB)s [7]. This configuration offers a good starting characteristic but suffers from low efficiency when compared to IM. An alternate design approach that covers the majority of line-start permanent magnet motor (LSPM) designs [8], [9] is applied to design of LSSynRM in [3] and [4]. Due to the presence of a permanent magnet in LSPM, its efficiency is higher than the IM. However, the efficiency of the LSSynRM that is designed through this method is not comparable to that of an IM because the optimal rotor composition for working in synchronous mode has not been achieved. The rotor slots introduce predetermined constraints for the reluctance rotor design. This, in turn, forms the main drawback of the induction rotor-based designs. The FBs are usually installed along the rotor slots to preserve d-axis flux.

Starting with a reluctance rotor as the base design, there will be no constraint due to the induction cage on the synchronous torque; consequently, the maximum saliency ratio is obtained in the steady state. In this approach, the design of the reluctance rotor imposes constraints on the cage location. Since the induction cage should not be installed on the flux path to prevent d-axis flux reduction; inserting the cage within the FBs becomes inevitable. However, limited induction cage location reduces the ability of the motor to start.

The LSSynRM reluctance rotor-based designs usually follow an optimal reluctance rotor pattern [10], [11]. If by installing the induction cage inside the FBs, the motor does not reach synchronism in the remaining space of the rotor iron, the induction cage will expand [12], thereby leading to a decrease in motor efficiency caused by the change in the optimal FBs' state [12].

In a previous work reported in [13] it is shown that the optimization problem of SynRM Rotor is a multimodal function, meaning that with different positioning of the FBs, one can obtain desirable performance for average torque and torque ripple. This paper seeks to use this concept for combined improvement of starting torque and high efficiency during steady state operation of LSSynRM. In this paper, the LSSynRM design is approached using the reluctance rotor-based technique. Furthermore, three various structures based on the order of thickness in flux barriers are selected as base design for LSSynRM. Following these selections, an adequate induction cage is designed for each variant. Rectangular bars are used in the design of the induction cage, and the synchronous reluctance rotor is designed to allow bars of the same width to be installed in the FBs thereby minimizing the change in the shape of the reference reluctance rotors. Consequently, the starting, and steady-state performances of the optimal motors are compared, and the best variant is selected.

II. LSSYNRM ANALYSIS

Analysis of LSSynRM performance is performed under steady-state and transient modes of operation as shown in Fig. 1. Under the steady state mode, a model that is excited using current sources is considered. Optimization is targeted towards maximizing the torque (efficiency) and minimizing the torque ripple while discarding the induction cage under steady state condition. In the transient mode, a voltage source model is applied to evaluate the motor synchronization capability by including the induction cage, inertia, and load torque. Although a steady-state performance becomes available at the end of this transient mode, a higher computational time would be required. In the following, the steady-state and transient operation of the LSSynRM [5], [12] are reviewed:

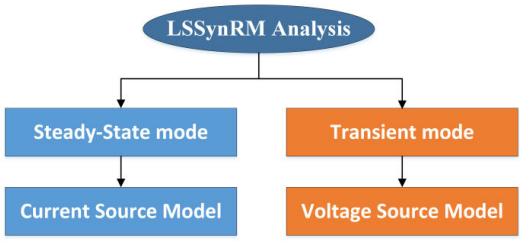

FIGURE 1. Steady-state and transient mode analysis of LSSynRM.

A. STEADY-STATE MODE OF OPERATION

The induction cage does not carry any current at synchronous speed. Therefore, the induction cage is removed at steady state mode, thereby reducing LSSynRM to a SynRM.

The average torque of a SynRM is given by (1) [5]:

$$T_{em}= \frac{3}{4}p(L_{sd}-L_{sq})I^2\sin(2\delta_i) \tag{1}$$

The maximum torque depends on the difference between the d-axis and q-axis inductances (i.e., magnetic saliency). Hence, torque maximization is yield by increasing the d-axis inductance and decreasing the q-axis inductance. The electromagnetic torque is determined using voltage source excitation by (2) [5]:

$$T_{em}=\frac{3}{2}p\frac{V^2}{2}\frac{(L_{sd}-L_{sq})}{\left(R_s^2+X_dX_q\right)^2}\left\{\begin{array}{l}\left(X_dX_q-R_s^2\right)\sin(2\delta_v)\\ +R_s\left(X_d-X_q\right)\\ -R_s\left(X_d+X_q\right)\cos(2\delta_v)\end{array}\right\} \tag{2}$$

An increase in the stator resistance decreases the maximum torque. In low-power motors, the stator resistance plays a dominant role [5]. If the stator resistance is neglected, the electromagnetic torque obtained with voltage excitation is similar to that of the current excitation expression (1).

To simulate the steady state, the motor speed is assumed to be constant and equal to the synchronous speed. This assumption eliminates the transient effects caused by the mechanical parameters. If a current source model is used for simulation, the steady-state currents will be directly applied to the stator phases. However, if a voltage source is used, the electromagnetic transients will take place due to the electromotive force, and it takes additional time to reach a steady-state condition. This time depends on the electrical and mechanical time constants of the motor. The behavior of a SynRM at synchronous speed is assessed by feeding a voltage source or current source in [14]. The results indicate that the current and torque of the SynRM obtained from voltage source and current source models are virtually identical at synchronous speed with a small difference caused by core losses [14]. This observation justifies the use of the current source supply in optimizing the performance of the machine at steady state.

B. TRANSIENT MODE

By assuming that the electrical and magnetic transients are faster than their mechanical counterparts, the dynamic electromagnetic torque of the LSSynRM is obtained based on a slip function expressed in (3) [12]:

$$T_{em}(s)=T_{cage}(s)+T_{rel}(s)\cos(2s\omega t-\gamma) \tag{3}$$

which consist of two components of cage torque ($\boldsymbol{T_{cage}}$) and reluctance torque ($\boldsymbol{T_{rel}}$). The reluctance torque component oscillates at twice the synchronous speed and is named the pulsating torque component. The cage torque component is the average torque component, which accelerates the rotor to near synchronous speed and is obtained using mechanical slip through (4) [12]:

$$T_{cage}=\frac{3}{2}\frac{p}{2}\frac{V_s^2s\omega}{(\omega_r+s\omega)^2}\left(\frac{R_{rd}L_{md}^2}{R_{rd}^2L_{sd}^2+s^2\omega^2(L_{sd}L_{rd}-L_{md}^2)^2}+\frac{R_{rq}L_{mq}^2}{R_{rq}^2L_{sq}^2+s^2\omega^2(L_{sq}L_{rd}-L_{mq}^2)^2}\right) \tag{4}$$

The magnitude of cage torque near synchronous speed is essential; if the cage does not provide the torque needed to derive the load at synchronous speed, the motor will continue to operate at exceeding speed oscillations and will be damaged. In the synchronization process, the magnitude of slip is small (i.e., $\boldsymbol{\omega_r}$ is close to $\boldsymbol{\omega}$), therefore, during synchronization, $\boldsymbol{T_{cage}}$ is simplified into Eq. (5) [12]:

$$T_{cage}=\frac{3}{4}p\frac{s_{sync}\bar{V}_s^2}{\omega}\left\{\frac{1}{R_{rd}}\left(\frac{L_{md}}{L_{sd}}\right)^2+\frac{1}{R_{rq}}\left(\frac{L_{mq}}{L_{sq}}\right)^2\right\} \tag{5}$$

symbol $\boldsymbol{s_{sync}}$ is the motor slip during synchronization. For successful synchronization, low values of $\boldsymbol{R_{rd}}$ and $\boldsymbol{R_{rq}}$ are required. Reducing $\boldsymbol{R_{rd}}$ meets the conditions of successful synchronization more effectively than reducing $\boldsymbol{R_{rq}}$; because in a well-designed synchronous reluctance motor, $\boldsymbol{L_{sq}}$ is much lower than $\boldsymbol{L_{sd}}$ and is close to the motor leakage inductance, making $\boldsymbol{(L_{md}/L_{sd})^2}$ more significant than $\boldsymbol{(L_{mq}/L_{sq})^2}$.

III. SYNRM DESIGN

A three phase balanced ac winding is used in this study. This stator winding belongs to an existing AC induction motor whose geometric specifications are listed in Table 1.

TABLE 1. Stator parameters.

Parameter	Unit	Value
Stack length	[mm]	60
Stator outer diameter	[mm]	152
Stator inner diameter	[mm]	93
Shaft diameter	[mm]	25
Air gap thickness	[mm]	0.3
Slot opening	[mm]	2.53
Slot numbers	-	36
Pole pairs	-	2
Turns per slot	-	74

Four FBs per pole are used in the design of the SynR rotor. An increase in the number of FBs, theoretically, would improve the torque profile. However, in practice, it would increase the shear surface of the sheet and damage the magnetic properties of the core.

The proposed motor has 36 stator slots, and 32 equivalent rotor slots, the largest slot/slot synchronous parasitic torque due to the 17th harmonic happens at the speed of -187.5rpm. This speed is not placed in the motoring mode of operation; therefore, there is no problem in starting process.

To avoid undesirable secondary armature reactions in the proposed motor, the stator winding is considered by star connection and without parallel path.

The Fluid shape is considered for FBs to yield maximum torque [15]. The angle and thickness of the FBs (W_{qi} and $\Delta\alpha_i$, Fig. 2) are the variables that determine the rotor shape. The angle of the FBs is an influential parameter that affects torque ripple, and its thickness impacts the average torque [16].

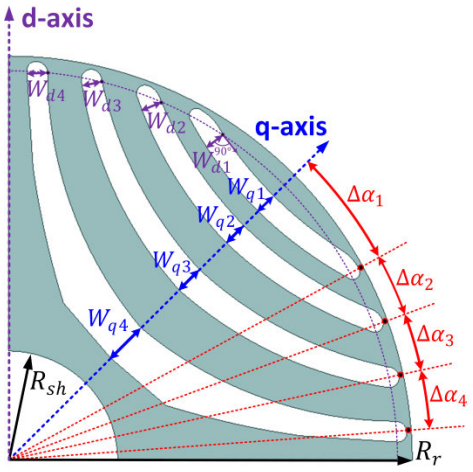

FIGURE 2. A SynR rotor with four FBs per pole and parameter definition.

A. SYNR ROTOR DESIGN FOR LINE-START APPLICATION

Finding an optimal design for a SynRM rotor is made possible through analytical methods. The analytical methods for design of FBs are usually based on the equal FBs' magnetic reluctance concept [17], [18]. The FBs' dimensions increase by increasing the distance from the rotor surface. In general, from an electromagnetic torque vantage point, an optimal SynRM rotor has the following features:

a. The shape of the FBs correspond to the distribution of flux lines (i.e., near the rotor surface, the flux lines are dense and become more distant in the central parts (i.e.$W_{di} < W_{qi}$)).
b. FBs that are close to the rotor surface are thin, and FBs that are distant from the surface are thicker (i.e.$W_{q1} < W_{q2} \ldots < W_{qn}$).

To improve synchronization, the following points regarding the location of induction cage need to be considered:

a. **The cage bars should be close to the rotor surface.** Due to stronger coupling with the stator magnetic field and smaller leakage inductance, the closer the cage bars to the rotor surface, the larger cage torque and hence a better synchronization capability.
b. **The cage bars should be close to the q axis.** The closer the bars to the q-axis, the higher synchronization torque due to the reduced resistance in the rotor d-axis (R_{rd}) [19].

Concentrating on the optimal position of the FBs and cage bars (for steady-state operation and increasing the synchronization capability, respectively) and considering the constraint that the cage bars should be installed inside the FBs (without disturbing the d-axis flux), one can note that there exists a conflict. This is evident because in an optimal SynRM rotor, less space is allocated for the FBs near the rotor surface and the q-axis, while to increase the synchronization capability, the bars must be close to the rotor surface and the q-axis.

Three different designs of SynRM rotor are illustrated in Fig. 3. In Fig. 3(a). the optimal reluctance rotor is sought using the analytical method [13], [20], where the thickness of FBs along the q-axis increases with an increase in FB's number (i.e. $W_{q1} < W_{q2} \ldots < W_{q4}$). In Fig. 3(b). the rotor with FBs that are equal in thickness along the $q$axis ($W_{q1} = W_{q2} \ldots = W_{q4}$) is illustrated. Finally, in Fig. 3 (c). the rotor with FBs equal in thickness along the d-axis (*i.e.*, $W_{d1} = W_{d2} \ldots = W_{d4}$). These choices are also known as the *Vagati, Wq-Equal,* and Wd-Equal rotors, respectively. In these three rotors, the insulation ratio along the q-axis is the same (K_{insq}= 0.4) and the FBs angle equals the rotor virtual slots ($\Delta\alpha_i = \pi/22$). This is the optimal condition for the stator with 36 slots according to the ($n_r = n_s + 4.$) rule [20].

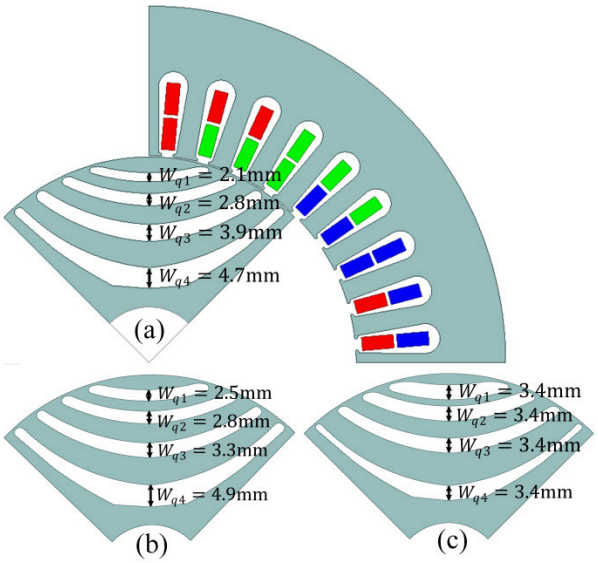

FIGURE 3. (a) Vagati rotor, (b) Wd-Equal rotor, and (c) Wq-Equal rotor.

The performance of these three rotors for the same stator current (2.3 A) is computed and compared in Table 2.

TABLE 2. Optimization constraints.

Parameter	Lower limit	Upper limit	Unit
$\Delta\alpha_1$	0.2	0.6	p.u.
$\Delta\alpha_i$ (i =2,…, N_b)	0.1	0.5	p.u.
$\sum_i^{N_b} \alpha_i < 1$ (i =1,..., N_b)			p.u.

The torque ripple of these rotors due to the constant angle of the FBs is virtually equal. The *Vagati* rotor has the highest torque; the *Wq-Equal* rotor produces the least torque,

TABLE 3. Performance comparison of different rotor types.

Rotor type	Torque [N.m]	Error % relative to Vagati	Torque Ripple %	Error % relative to Vagati
Vagati	6.40	0.00	18.64	0.00
Wd-Equal	6.37	0.46	18.17	-0.52
Wq-Equal	5.99	6.40	20.91	2.27

although it allocates more space near the rotor surface for the FBs. Though there exists a negligible difference between *Vagati* and *Wd-Equal* rotor in terms of steady-state performance, the *Wd-Equal* rotor has more empty space near the rotor surface than the *Vagati* rotor.

Since it is the objective of this research to design a high-efficiency motor for LSSynRM application, *Wd-Equal* shape is selected in design to effectively reduce the rotor resistances. As shown in section IV, this configuration also makes it easier to compare line-start rotors. The design problem of the SynRM rotor has many local optima [13]; consequently, by applying different combinations of angles and thicknesses of FBs, the proper performance in terms of torque and torque ripple can be achieved.

Fig. 4. shows the design process of LSSynRM. The algorithm is separated into two stages for SynRM and induction cage design. Starting with SynRM design to determine the optimal angle of FBs with the least torque ripple, the method proposed by [13] and [21] is adopted, which combines conformal mapping and magnetic equivalent circuit for modeling and uses a multimodal optimization algorithm. After determining the optimal angle of the FBs, by changing the insulation ratio, the thickness of the FBs is adjusted to allow their installation in the cage bars with the same size. According to the Wd-Equal pattern, this will allow for obtaining the maximum average torque. In the next stage, the optimal SynRM Rotors are considered for induction cage design. Width of the cage bars are increased until the motor can successfully synchronize the load. Clearly, the rotor with minimum copper consumption is selected for manufacturing.

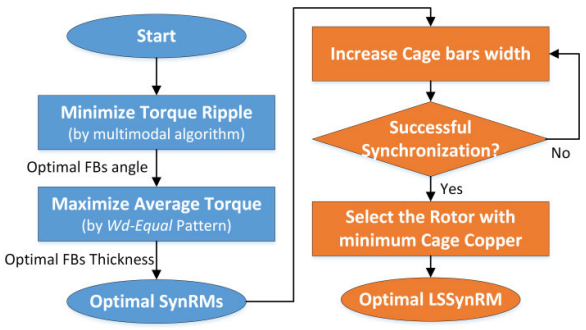

FIGURE 4. Design flowchart: (left) SynRM design and (right) cage design.

The angles of the three optimal rotors in terms of torque ripple are tabulated in Table 4.

TABLE 4. Optimal FB angles obtained through the analytical method.

Rotor name	$\Delta\alpha_1$ [deg]	$\Delta\alpha_2$ [deg]	$\Delta\alpha_3$ deg]	$\Delta\alpha_4$ deg]
A	20.50	7.52	7.56	7.16
B	15.30	14.00	7.65	5.85
C	16.30	7.83	8.15	8.73

By fixing the FBs angle, the location of the rotor magnetic potential drop remains constant, making the torque ripple almost constant as well. The insulation ratio is changed by keeping the FBs angles constant, and FE analysis is used for simulation. The average torque and peak-to-peak torque of rotors A, B, and C are shown in Figs 5- 6, respectively.

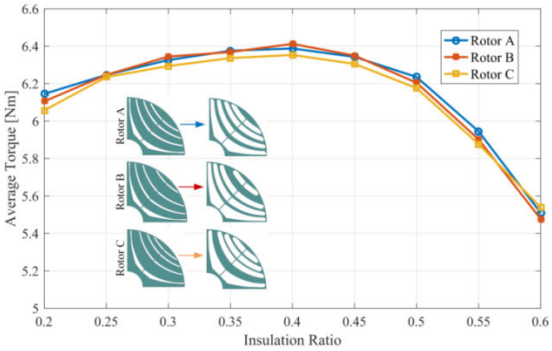

FIGURE 5. Effect of increasing insulation ratio on average torque.

An increase in the insulation ratio from 0.2 increases the average torque. This is due to the fact that as the thickness of the FBs increases, the inductance of the q-axis decreases while there is still enough iron to pass the d-axis flux. The maximum torque is obtained for three motors at 0.4 isolation ratio. Further increase in the FBs thickness reduces the d-axis flux and average torque.

As observed in Fig. 6. a variation in the insulation ratio between 0.2 and 0.5 leads to an almost constant peak-to-peak torque in these three motors. A further increase in insulation

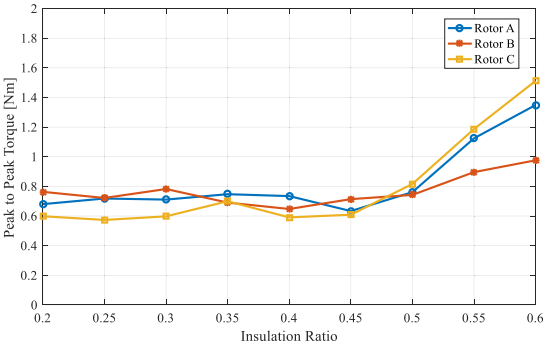

FIGURE 6. Effect of increasing insulation ratio on torque ripple.

ratio (within the range of 0.6 to 0.8) leads to core saturation due to the B-H (i.e., magnetization) curve's nonlinearity. This leads to an increase in torque ripple.

The optimal rotors A, B, and C, at 0.4 insulation ratio, are shown in Fig. 7, and their average torque and ripple values per equal stator current are compared in Table 5.

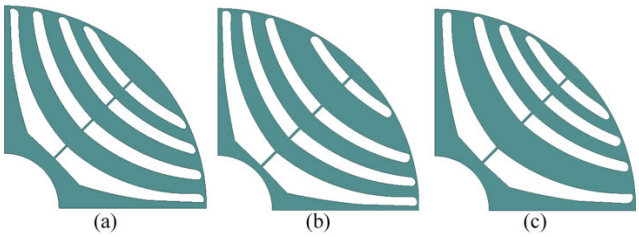

FIGURE 7. Optimal SynRM rotors: (a) Rotor A, (b) Rotor B, and (c) Rotor C.

TABLE 5. Performance comparison of optimal SynRMs.

Rotor type	Current [A]	Current Angle [deg.]	Torque [N.m]	Torque Ripple %
A	2.3	61	6.39	11.53
B	2.3	61	6.41	10.07
C	2.3	61	6.38	9.39

The steady-state operations of the rotors are similar. Their aggregate maximum torque and torque ripple differences are about 2% and 0.5%, respectively. In the remaining parts of the paper, SynRM rotors A, B, and C constitute the design basis of the line-start motor.

IV. INDUCTION CAGE DESIGN

The LSSynRM design is load-dependent, the behavior of which during the start-up affects the motor synchronization capability. Common loads based on their torque-speed characteristic are categorized as [23]; 1) light-duty, 2) medium-duty, 3) heavy start-duty, and 4) heavy-duty. The typical torque-speed characteristics of different loads are shown in Fig. 8. In this study, the medium-duty load is considered for the induction cage design, where fans, blowers, centrifugal pumps, and compressors are prime targets. Torque dependency to the square of the speed and a starting torque between

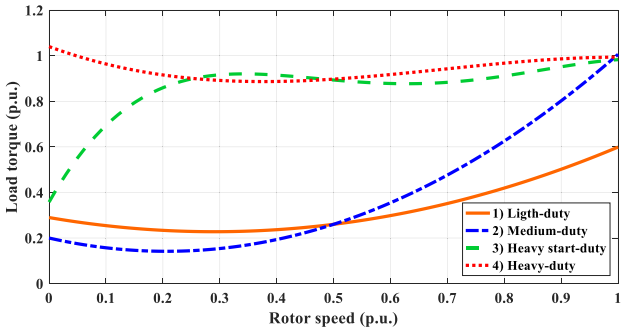

FIGURE 8. Torque-speed characteristic of different loads [22].

10 to 40% of the rated torque defines the medium-duty load characteristic [23]. In all simulations, the starting torque is 40% of the rated torque, and the total inertia is twice as large when compared to the motor inertia.

In the case of low-power LSSynRMs, the voltage drop due to the stator resistance is not negligible during the start. The reduced voltage will negatively affect both reluctance and induction torque for synchronization. The parameter that can help synchronization is the rotor resistance. In the case of the proposed LSSynRM, even with completely filled flux barriers by aluminum and considering the available space for the end rings, the motor could not successfully synchronize the desired load by simulation. So the copper bars are considered for induction cage design.

Rectangular and circular bars are the two commonly used shapes considered for the cage design, which will be compared in the following section.

A. CAGE DESIGN WITH RECTANGULAR BARS

The thickness of all cage bars is set to 2.5 mm; the distance from the rotor surface is 1.5 mm to prevent bars from changing the flux carrier's path at the end, which is highly influential on torque ripple. As observed in Fig. 9, the bar widths are increased from 4 mm using a 1 mm step until the motor can synchronize the load. By doing so, the minimum copper consumption volume is obtained to create a cage that can synchronize the desired load.

The speed-time characteristics of motors for the three different selections of the bar width and equal end ring are shown in Figs. 10, 11, and 12, respectively. As to motor A, the average speed increases as the width of the bars increases from 4 to 11 mm. Notably, there are sharp oscillations in speed. When the bar width reaches 12 mm, the motor can successfully synchronize and damp speed oscillations. As to motor B, the synchronization capability is obtained for bars of 11 mm in width, which are reduced by 1 mm compared to motor A. Motor C with an 8 mm bar width, which is the lowest volume compared to other motors, can synchronize the load.

This advantage is explained by the fact that the angle of the FBs in rotor C is closer to the q-axis. Cage bars close to the q-axis decrease the rotor resistance in the d-axis more effectively and increase the motor synchronization capability [19]. Therefore, to minimize cage material, it is recommended that among different options for LSSynRM applications, the one with closest FB angles to q-axis to be selected.

The results of the losses calculated in steady-state mode for motors with rectangular bars are tabulated in Table 6.

According to Table 6, motors A, B, and C have the highest rotor ohmic loss among rectangular cage designs, respectively. The rotor ohmic loss of motor A is twice as large compared to that of motor C. In motors A and B, more cage volume is exposed to flux harmonics because the cage bars are more extensive, leading to more significant eddy current losses; hence motor C has the highest efficiency.

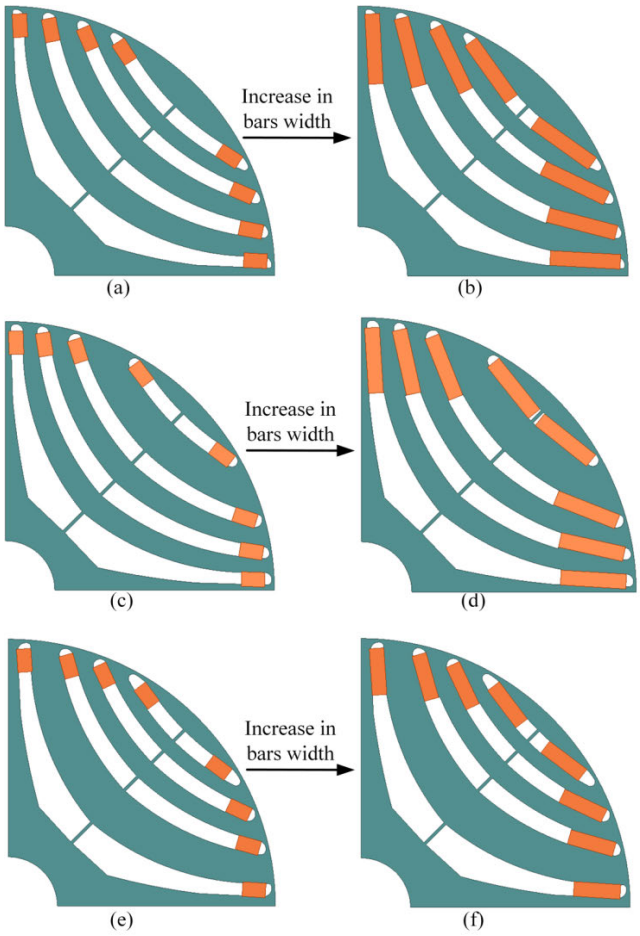

FIGURE 9. Rotor A with 4mm (a) and 12 mm (b) bars, Rotor B with 4mm (c) and 11 mm (d) bars, Rotor C with 4mm (e) and 8 mm (f) bars.

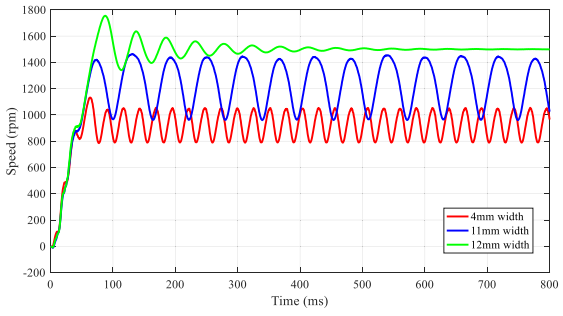

FIGURE 10. Motor A start-up, rectangular bars.

B. CAGE DESIGN WITH CIRCULAR BARS

Circular bars are beneficial in the case of eddy current loss. Similar to rectangular bars cage, the size of all circular bars is the same here. Moreover, they are installed inside the FBs at the same distance from the rotor surface. As observed in Fig. 13, the diameter of the bars is increased from 3.6 mm by steps of 0.1 mm until the motor can synchronize the load. The speed-time curves for three different cases of bar diameter are shown in Fig. 14. When the diameter of the bars reaches 5 mm, the motor can synchronize the load, which is approximately equal in cross-section to 8 mm long rectangular bars.

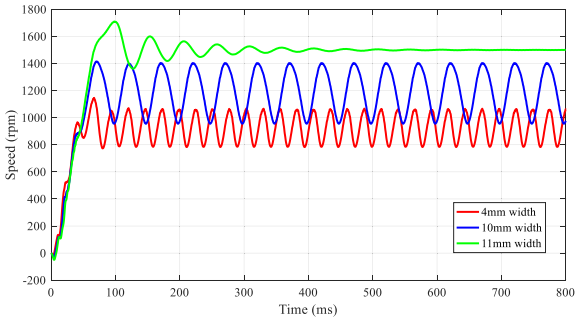

FIGURE 11. Motor B start-up, rectangular bars.

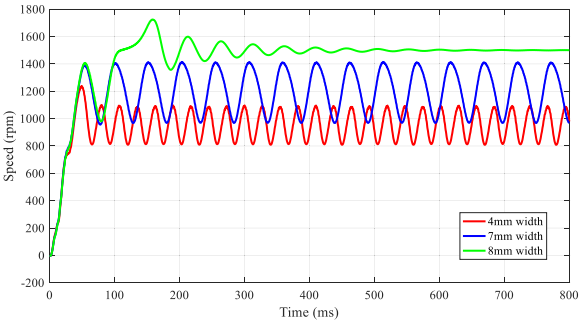

FIGURE 12. Motor C start-up, rectangular bars.

TABLE 6. FE result of LSSynRMs at 1kw output, steady-state mode.

Parameter	Unit	Motor-A	Motor-B	Motor-C
Voltage	[V]	380	380	380
Current	[A(rms)]	2.33	2.39	2.31
Stator ohmic loss	[W]	74.0	78.2	72.7
Rotor ohmic loss	[W]	15.1	13.2	7.5
Core loss	[W]	52.1	53.6	53.9
Windage loss	[W]	10.0	10.0	10.0
Total loss	[W]	152.7	154.9	144.4
Efficiency	%	86.75	86.59	87.38

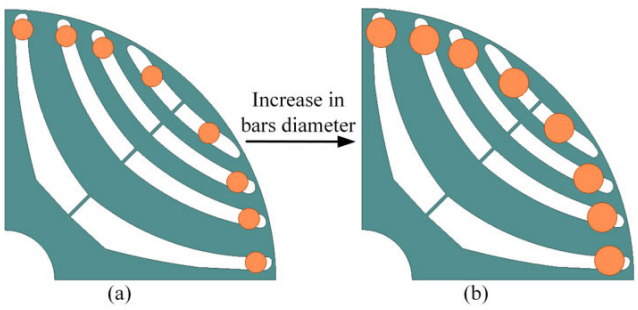

FIGURE 13. Motor C, circular bars, 3.6 mm (a) and 5 mm (b) diameter.

The loss calculation results for steady-state modes for motor C with rectangular and circular bars are tabulated in Table 7.

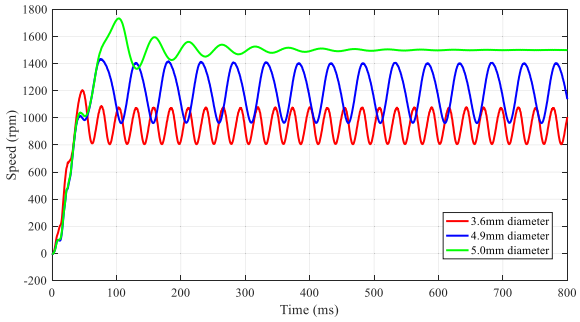

FIGURE 14. Motor C start-up, circular bars.

TABLE 7. LSSynRM performance with rectangular and circular Bars.

Parameter	Unit	Circular bar motor	Rectangular bar motor
Voltage	[V]	380	380
Current	[A(rms)]	3.48	2.31
Stator ohmic loss	[W]	180.6	72.7
Rotor ohmic loss	[W]	6.3	7.5
Core loss	[W]	55.78	53.9
Windage loss	[W]	10.0	10.0
Total loss	[W]	251.8	144.1
Efficiency	%	79.88	87.38

Although the cross-sections of the bars are equal in both cases and successful synchronization is obtained, the motor's efficiency with circular bars is reduced by 7.5% compared to the rectangular bars. The ohmic rotor loss is lower in the motor with circular bars, though these bars increase the stator ohmic loss. Circular bars reduce the saliency ratio by blocking the d-axis flux path, and to overcome this, the stator current must be increased, which would lead to a decrease in motor efficiency and an increase in iron losses.

The flux density distribution in motor C with rectangular and circular bars under steady-state nominal load is shown in Fig. 15. Because FBs in a rotor with circular bars are thin near the rotor surface, the bars enter the flux guides region and narrow the d-axis flux path, thus, saturate the core in these regions. Reduction in d-axis inductance leads to a decrease in motor efficiency under synchronous operating conditions.

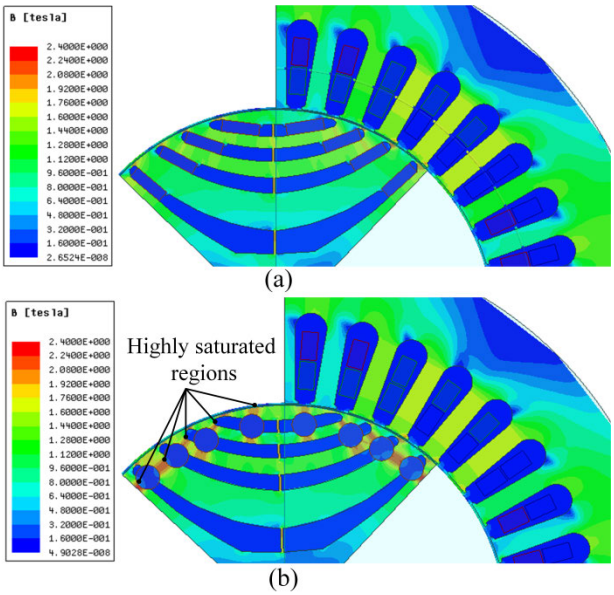

FIGURE 15. Flux density in motor-C with (a) rectangular bar and (b) circular bar cage.

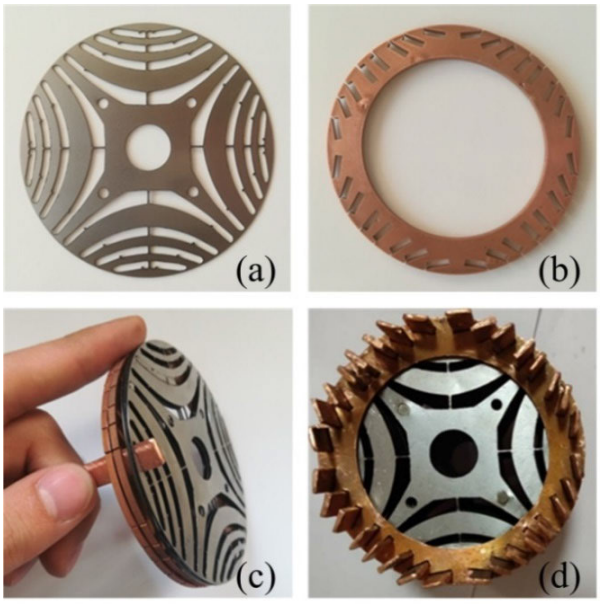

FIGURE 16. (a) SynRM lamination, (b) A short circuit ring, (c) Placing a bar in rotor, (d) Rotor cage before brazing.

V. EXPERIMENTAL RESULTS

A sample lamination of rotor C developed using laser cut is shown in Fig. 16 (a). Some holders are attached among the bars for better support in the final rotor shape. Some bolts are added to the final rotor design for the mechanical integrity of the laminations. Their location is selected near the shaft where the flux density is low enough, so they do not change the flux density pattern. As observed

in Figs. 16 (b) and (c), a 2.5mm thick copper sheet is applied to make the bars and the short circuit rings; the short circuit Rings are obtained by the wire cutting method. Each side of the rotor has three layers of 2.5mm rings connected to the bars by brazing. The installation of the bars and rings before brazing is shown in Fig. 16(d). To compare the simulation results with the obtained measurements, a test-bed is developed and shown in Fig. 17. The test motor is connected to a 4.65kW DC generator through an inline rotary torque meter with a 20 Nm nominal capacity and 0.1% accuracy. The currents and voltages of a three-phase motor are recorded through the Unilyzer 902 power analyzer. The motor shaft is extended from the back of the motor to measure the motor's transient speed and rotor position via an encoder.

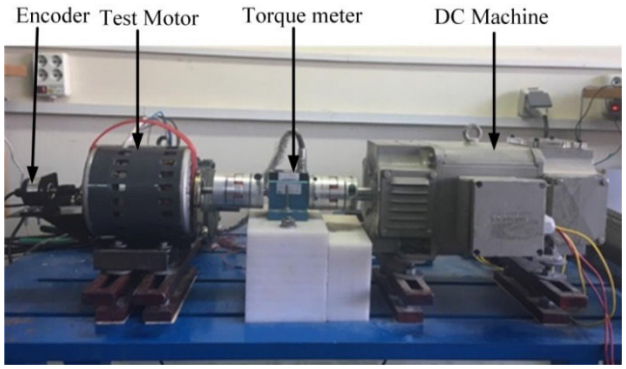

FIGURE 17. Testbed.

TABLE 8. Steady-state performance simulation vs. measurement.

Parameter	*Unit*	Simulation	Measurement
Line Voltage	[V]	380.0	381.2
Voltage THD	%	0.00	4.95
Phase Current	[A]	2.31	2.42
Current THD	%	1.67	2.88
Speed	[RPM]	1500.0	1500.5
Mech Power	[W]	1000.0	1010.5
Electric Power	[W]	1144.4	1165.3
Power Factor	-	0.753	0.729
Efficiency	%	87.38	86.71

FIGURE 18. Cross section view of the soldered the squirrel cage bars.

A. STEADY STATE

The motor performance in the steady-state mode under a nominal voltage of 380 volts is shown in Table 8. The LSSynRM motor is connected directly to the mains, and the measurements are recorded subject to the rated torque. There exists a good agreement between the simulation and laboratory results.

The voltage applied to the motor is shown in Fig. 19; the stator currents at steady state are shown in Fig. 20. The THD of the steady-state current is 4.95%, partly because the supply voltage THD reaches 2.88%.

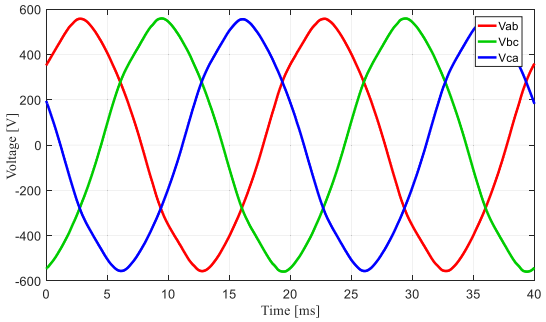

FIGURE 19. Experimentally recorded Line voltage at steady state.

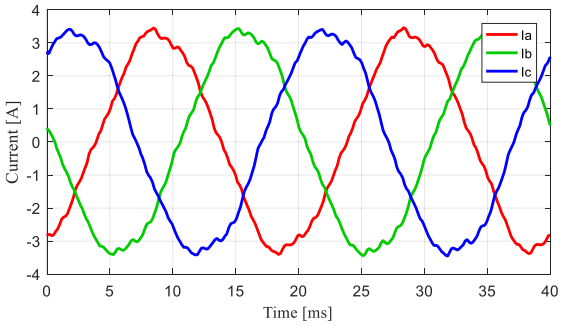

FIGURE 20. Experimentally recorded steady-state phase currents.

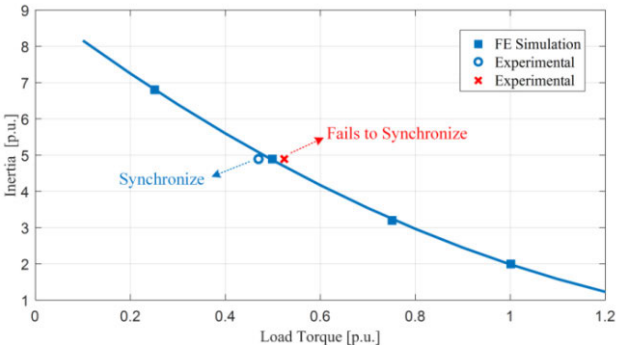

FIGURE 21. LSSynRM Synchronization capability.

In terms of assembly for the prototypes, the squirrel cage bars are soldered to the end ring as can be seen in Fig. 18. First, the end ring and bars are heated, and then the solder wire is applied to the junction points. The strength of the connections has been checked by visual evaluation.

B. SYNCHRONISM CAPABILITY

The motor starts under different loads on the DC generator to assess the synchronization capability. The motor is designed to drive a load of one kilowatt with an inertia equal to its inertia (0.0033Kgm2). However, the DC machine coupled to the motor has about four times the motor's inertia; therefore, the magnitude of successfully synchronized load is reduced subject to these conditions. The LSSynRM synchronization capability is shown in Fig. 21. The maximum torque that successfully synchronizes the motor for different inertia is

obtained through FE simulation. The points indicated by the symbols o and x in Fig. 21 indicate the successful and unsuccessful synchronization attempts throughout the test, respectively. The results of torque and speed measurement for

Since a per unit scale for the vertical axes in Fig. 21 is chosen, it is important to note that the base value for inertia is the rotor inertia (0.0033kgm2), and the base value for torque is the nominal torque (6.37 Nm.). Successful and unsuccessful synchronization are shown in Fig. 22 and 23, respectively. There exists a good agreement between the test results and the simulation.

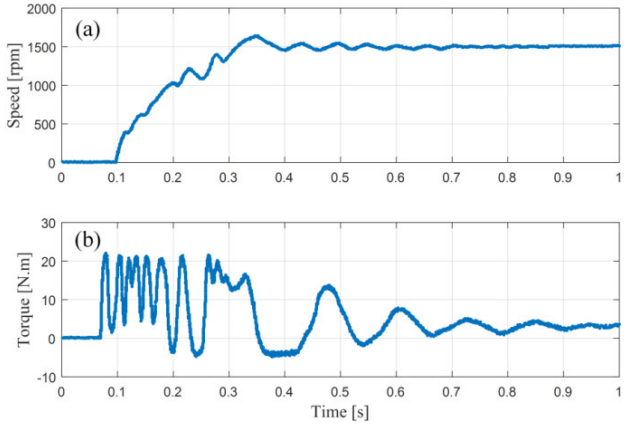

FIGURE 22. Experimentally recorded successful synchronization, (a) Speed (b) Torque.

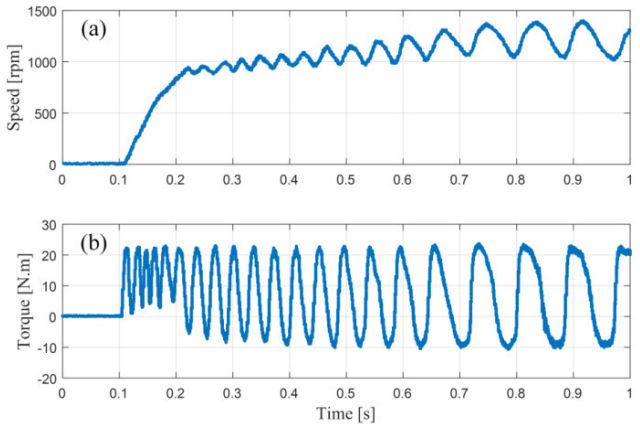

FIGURE 23. Experimentally recorded failed synchronization, (a) Speed (b) Torque.

Figs. 24 and 25 illustrate the calculated torque and speed for the purpose of comparison with those from measurement. It must be noted that the torquemeter has a fairly limited bandwidth and some of the high frequency noise has been filtered during the measurement. Transient waveforms of currents from simulation and experiments under successful synchronization are shown in Figs. 26 and 27 respectively.

For successful synchronization, multiple tests are performed to record the transient current waveforms using the

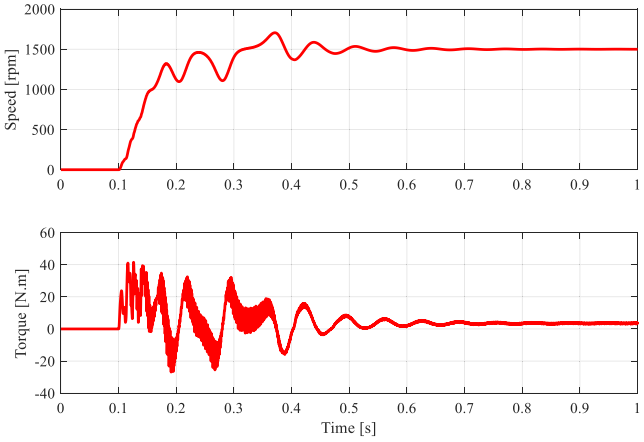

FIGURE 24. Simulation results for the successful synchronization experimentally simulation results for successful synchronization,) Speed (top) Torque(bottom).

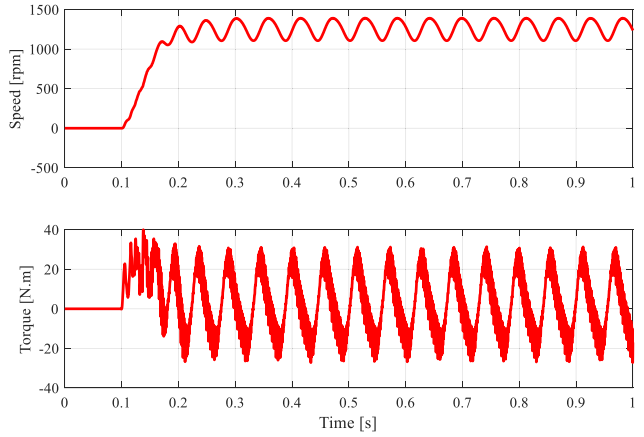

FIGURE 25. Simulation results for failed synchronization, Speed (top) Torque (bottom).

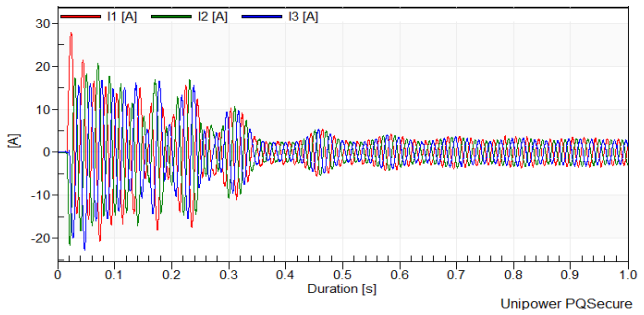

FIGURE 26. Experimentally recorded current waveforms for a successful synchronization.

power analyzer. Due to the low power of the motor, it is difficult to record the transient current using a power analyzer.

For failed synchronization, unfortunately, the results of the experiment could not recorded. The failed synchronization test is a very harmful test that can damage the motor and coupling structures and cannot be repeated.

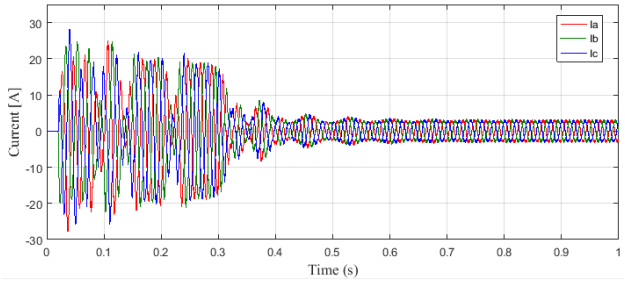

FIGURE 27. Simulated current waveforms for a successful synchronization.

Finally, it must be mentioned that this line start motor is targeted for applications in fans, blowers, centrifugal pumps, and compressors which are referred to as medium-duty loads. These loads exhibit a starting torque that is about 10-40% of their rated load and their torque rises with the square of the speed [23].

VI. CONCLUSION

The results presented in this paper illustrate the importance of SynRM selection for Line-Start Applications. Three optimal synchronous reluctance rotors are studied to design the LSSynRM, and the results indicate that although different synchronous reluctance rotors operate under similar steady-state conditions, they provide different transient modes by placing cage bars of the same size in their FBs. The rotor with FBs closest to the q-axis has more synchronization capability. The comparison of rotor cages with rectangular and circular bars indicates that they have the same copper consumption rate in achieving the same synchronization capability, while the cages with rectangular bars show better steady-state performance than circular bars due to their adaptation to the shape of the FBs.

REFERENCES

[1] J. Tampio, T. Känsäkangas, S. Suuriniemi, J. Kolehmainen, L. Kettunen, and J. Ikäheimo, "Analysis of direct-on-line synchronous reluctance machine start-up using a magnetic field decomposition," *IEEE Trans. Ind. Appl.*, vol. 53, no. 3, pp. 1852–1859, May 2017.

[2] M. Gamba, G. Pellegrino, A. Vagati, and F. Villata, "Design of a line-start synchronous reluctance motor," in *Proc. Int. Electric Mach. Drives Conf.*, May 2013, pp. 648–655.

[3] Q. Smit, A. Sorgdrager, and R. Wang, "Design and optimisation of a line-start synchronous reluctance motor," in *Proc. 24th Southern Afr. Universities Power Eng. Conf.*, 2016.

[4] V. Aguba, M. Muteba, and D. V. Nicolae, "Transient analysis of a start-up synchronous reluctance motor with symmetrical distributed rotor cage bars," in *Proc. IEEE AFRICON*, Sep. 2017, pp. 1290–1295, doi: 10.1109/AFRCON.2017.8095668.

[5] A. Kersten, "Efficiency investigation of line start synchronous reluctance motors," M.S. thesis, Dept. Energy Environ., Chalmers Univ. Technol., Göteborg, Sweden, 2017.

[6] M. Gamba, E. Armando, G. Pellegrino, A. Vagati, B. Janjic, and J. Schaab, "Line-start synchronous reluctance motors: Design guidelines and testing via active inertia emulation," in *Proc. IEEE Energy Convers. Congr. Expo. (ECCE)*, Sep. 2015, pp. 4820–4827.

[7] S. T. Boroujeni, N. Bianchi, and L. Alberti, "Fast estimation of line-start reluctance machine parameters by finite element analysis," *IEEE Trans. Energy Convers.*, vol. 26, no. 1, pp. 1–8, Mar. 2011.

[8] F. J. H. Kalluf, C. Pompermaier, M. V. F. da Luz, and N. Sadowski, "Modelling of a line-start permanent magnet motor using finite element method," in *Proc. 5th IET Int. Conf. Power Electron., Mach. Drives (PEMD)*, May 2010.

[9] M. N. Azari and M. Mirsalim, "Line-start permanent-magnet motor synchronisation capability improvement using slotted solid rotor," *IET Electr. Power Appl.*, vol. 7, no. 6, pp. 462–469, Jul. 2013.

[10] H.-C. Liu and J. Lee, "Optimum design of an IE4 line-start synchronous reluctance motor considering manufacturing process loss effect," *IEEE Trans. Ind. Electron.*, vol. 65, no. 4, pp. 3104–3114, Apr. 2018.

[11] A. Kersten, Y. Liu, D. Pehrman, and T. Thiringer, "Rotor design of line-start synchronous reluctance machine with round bars," *IEEE Trans. Ind. Appl.*, vol. 55, no. 4, pp. 3685–3696, Jul. 2019, doi: 10.1109/TIA.2019.2914010.

[12] M. Gamba, G. Pellegrino, and A. Vagati, "Design of non conventional synchronous reluctance machine," M.S. thesis, Politecnico di Torino, Dept. Energy, 2017.

[13] M. Farhadian, M. Moallem, and B. Fahimi, "Multimodal optimization algorithm for torque ripple reduction in synchronous reluctance motors," *IEEE Access*, vol. 10, pp. 26628–26636, 2022.

[14] R. R. Moghaddam, "Synchronous reluctance machine (SynRM) in variable speed drives (VSD) applications," M.S. thesis, KTH Roy. Inst. Technol., Stockholm, Sweden, 2011.

[15] M. Gamba, G. Pellegrino, and F. Cupertino, "Optimal number of rotor parameters for the automatic design of synchronous reluctance machines," in *Proc. Int. Conf. Electr. Mach. (ICEM)*, Sep. 2014, pp. 1334–1340, doi: 10.1109/ICELMACH.2014.6960355.

[16] R.-R. Moghaddam and F. Gyllensten, "Novel high-performance SynRM design method: An easy approach for a complicated rotor topology," *IEEE Trans. Ind. Electron.*, vol. 61, no. 9, pp. 5058–5065, Sep. 2014.

[17] A. Vagati, G. Franceschini, I. Marongiu, and G. P. Troglia, "Design criteria of high performance synchronous reluctance motors," in *Proc. Conf. Rec. IEEE Ind. Appl. Soc. Annu. Meeting*, Oct. 1992, pp. 66–73, doi: 10.1109/IAS.1992.244463.

[18] Y. Wang, G. Bacco, and N. Bianchi, "Geometry analysis and optimization of PM-assisted reluctance motors," *IEEE Trans. Ind. Appl.*, vol. 53, no. 5, pp. 4338–4347, Sep. 2017, doi: 10.1109/TIA.2017.2702111.

[19] S. T. Boroujeni, M. Haghparast, and N. Bianchi, "Optimization of flux barriers of line-start synchronous reluctance motors for transient- and steady-state operation," *Electr. Power Compon. Syst.*, vol. 43, no. 5, pp. 594–606, Mar. 2015.

[20] A. Vagati, M. Pastorelli, G. Francheschini, and S. C. Petrache, "Design of low-torque-ripple synchronous reluctance motors," *IEEE Trans. Ind. Appl.*, vol. 34, no. 4, pp. 758–765, Jul. 1998, doi: 10.1109/28.703969.

[21] M. Farhadian, M. Moallem, and B. Fahimi, "Analytical calculation of magnetic field components in synchronous reluctance machine accounting for rotor flux barriers using combined conformal mapping and magnetic equivalent circuit methods," *J. Magn. Magn. Mater.*, vol. 505, Jul. 2020, Art. no. 166762.

[22] C.-T. Liu, P.-C. Shih, Z.-H. Cai, K. Yang, S.-C. Yen, H.-N. Lin, Y.-W. Hsu, T.-Y. Luo, and S.-Y. Lin, "Designs of a four-in-one laminated electrical steel rotor structure for application-oriented synchronous reluctance motors," *IEEE Trans. Ind. Appl.*, vol. 55, no. 4, pp. 4389–4397, Jul. 2019.

[23] K. Agrawal, *Industrial Power Engineering Handbook*. Amsterdam, The Netherlands: Elsevier, 2001.

MOEIN FARHADIAN received the M.Sc. degree in electrical engineering from the Isfahan University of Technology, Iran, in 2017, where he is currently pursuing the Ph.D. degree. His research interests include electric machine modeling, analysis, and design optimization using advanced analytical and numerical methods with a special interest in synchronous and switched reluctance motors.

MEHDI MOALLEM (Senior Member, IEEE) received the Ph.D. degree in electrical engineering from Purdue University, West Lafayette, IN, USA, in 1989. Since 1990, he has been with the Department of Electrical and Computer Engineering, Isfahan University of Technology, Isfahan, Iran. He has authored more than 150 peer-reviewed journal and conference papers. His current research interests include the design and optimization of electromagnetic devices, application of advanced analytical and numerical techniques in electric machine modeling, analysis, and diagnosis, and power quality.

BABAK FAHIMI (Fellow, IEEE) received the B.S. and M.S. degrees (Hons.) in electrical engineering from the University of Tehran, Iran, in 1991 and 1993 respectively, and the Ph.D. degree in electrical engineering from Texas A&M University, in 1999. He has been active in research on electric machines and drives over the past 30 years. He has coauthored more than 375 peer-reviewed articles and holds 22 U.S. patents. He has been an advisor for 36 Ph.D. students and 30 M.S. students. He is a fellow of IEEE for the contributions to modeling of adjustable-speed motor drives.

BEHZAD MIRZAEIAN DEHKORDI was born in Shahrekord, Iran, in 1966. He received the B.Sc. degree in electronics engineering from Shiraz University, Iran, in 1985, and the M.Sc. and Ph.D. degrees in power engineering from the Isfahan University of Technology (IUT), in 1994 and 2000, respectively. In September 2002, he joined the Department of Electrical Engineering, University of Isfahan, where he is currently a Professor of electrical engineering. He was a Visiting Professor with the Power Electronic Laboratory, Seoul National University (SNU), South Korea, from March 2008 to August 2016. His research interests include power electronics and motor drives, intelligent systems, and renewable energy.

MEHDI SAHEBZAMANI was born in Ardabil, Iran, in 1971. He received the B.Sc. degree in electrical engineering from the Amirkabir University of Technology, in 1994, and the M.Sc. degree in power engineering from the Isfahan University of Technology (IUT), in 1996. He is currently the CEO of Kia Electromotor Part (KEP) Company, Tehran, Iran.